Available online at www.sciencedirect.com

ScienceDirect

www.elsevier.com/locate/jmbbm

Research Paper

Passive skeletal muscle response to impact loading: Experimental testing and inverse modelling

Michael Takaza[a,*], *Kevin M. Moerman*[b], *Ciaran K. Simms*[a]

[a]*Centre for Bioengineering, School of Engineering, Parsons Building, Trinity College, Dublin 2, Ireland*
[b]*Academic Medical Centre, Department of Radiology, Meibergdreef 9, 1100 DD Amsterdam, The Netherlands*

ARTICLE INFO

Article history:
Received 9 November 2012
Received in revised form
18 April 2013
Accepted 20 April 2013
Available online 9 May 2013

Keywords:
Muscle compression
Impact loading
Mechanical & deformation behaviour
Inverse analysis

ABSTRACT

Appropriate mechanical representation of passive muscle tissue is crucial for human body impact modelling. In this paper the experimental and modelling results of compressive loading of freshly slaughtered porcine muscle samples using a drop-tower testing rig are reported. Fibre and cross-fibre compression tests at strain rates varying from 11,600%/s to 37,800%/s were performed. Experimental results show a nonlinear stress–stretch relationship as well as a clear rate dependency of the stress. The mean (standard deviation) engineering stress in the fibre direction at a stretch of 0.7 was 22.47 kPa (5.34 kPa) at a strain rate of 22,000%/s and 38.11k Pa (5.41 kPa) at a strain rate of 37,800%/s. For the cross-fibre direction, the engineering stresses were 5.95 kPa (1.12 kPa) at a strain rate of 11,600%/s, 25.52 kPa (5.12 kPa) at a strain rate of 22,000%/s and 43.66 kPa (6.62 kPa) at a strain rate of 37,800%/s. Significant local strain variations were observed, as well as an average mass loss of 8% due to fluid exudation, highlighting the difficulties in these kinds of tests. The inverse analysis shows for the first time that the mechanical response in terms of both applied load and tissue deformation for each of the strain rates can be captured using a 1st order Ogden hyperelastic material law extended with a three-term quasilinear viscoelastic (QVL) expansion to model viscoelastic effects. An optimisation procedure was used to derive optimal material parameters for which the error in the predicted boundary condition force at maximum compression was less than 3% for all three rates of testing (11,600%/s, 22,000%/s and 37,800%/s). This model may be appropriate for whole body impact modelling at these rates.

1. Introduction

Skeletal muscle accounts for about 40% of body mass (Chomentowski et al., 2011; Salem et al., 2006) and an understanding of its mechanical properties is therefore important for impact biomechanics research. However, the multi-axial compressive properties of fresh skeletal muscle at rates experienced during typical sports and automotive impacts are not well understood (Van Loocke et al., 2009). Therefore, although finite element human body models including muscle tissue are routinely used in impact biomechanics research, their utility remains limited mainly by uncertainties in the constitutive representation of the soft tissues.

Skeletal muscle is composed of about 70–80% water, 3% fat and 10% collagen (Vignos and Lefkowitz, 1959). It exhibits a fibre-oriented structure, with each muscle composed of fascicles

*Corresponding author. Tel.: +353 1 896 2978.
E-mail addresses: takazam@tcd.ie, m.takaza1@gmail.com (M. Takaza).

1751-6161/$ - see front matter © 2013 Elsevier Ltd. All rights reserved.
http://dx.doi.org/10.1016/j.jmbbm.2013.04.016

containing bundles of fibres which themselves are composed of parallel bundles of myofibrils. There is a dense network of connective tissues which surrounds groups of fibres and this has a hierarchical structure. Arising from this structure, skeletal muscle presents a nonlinear elastic, non-homogeneous, anisotropic and viscoelastic behaviour (Van Loocke et al., 2006, 2008, 2009).

The need for experimental data for impact biomechanics applications can be assessed by the following order of magnitude comparison: in a 48 km/h unrestrained frontal vehicle impact, assuming the occupant's body strikes the vehicle interior at 48 km/h, the tissue compression rate is 13.33 m/s. For a mid-body region muscle thickness of 5 cm, this represents a compression rate of around 25,000%/s (Van Loocke et al., 2009), but combined fibre/cross-fibre data at these rates are not generally available.

Very high rate tests (up to 100,000%/s) have been performed by several researchers, but they have not assessed the effects of fibre direction (Van Sligtenhorst et al., 2006; McElhaney, 1966)). Song et al. (2007) did assess the influence of fibre direction for load ranges between 0.7%/s and 370,000%/s (Song et al., 2007), but their data surprisingly show identical responses for strain rates of 0.7%/s and 7%/s. Others have tested volunteers and cadavers (Dhaliwal et al., 2002; Muggenthaler et al., 2008) but, in the absence of inverse modelling, this approach only yields structural parameters. Chawla et al. (2009) performed compressive impact tests and inverse analysis on surgical scraps of human tissue which had been frozen and then thawed and the state of rigor mortis is unfortunately unknown in these tests.

Finite element analysis (FEA) models for whole body impact simulations have been developed in order to understand injury mechanisms (Maeno and Hasewaga, 2001; Kuwahara et al., 2007; Han et al., 2012). However these models depend on the chosen constitutive models for the tissues and their parameters, and both of these remain a significant limitation for whole body impact simulations. In most cases, an isotropic linear elastic model is used with parameters based on transverse compressive testing only. However, this is insufficient to model the anisotropic response observed in quasi-static testing (Van Loocke et al., 2006) as well as dynamic testing (Van Loocke et al., 2008, 2009). Thus, compressive testing in multiple directions at the relevant rates is required to guide appropriate model development. The attendant rate dependency of skeletal muscle also needs to be incorporated into these FEA models. Accordingly, measuring the rate dependent multi-axial compressive properties of skeletal muscle and providing input data for constitutive models at rates relevant to automotive accidents are important research goals and these form the focus of this paper.

2. Methods

2.1. *Experimental procedures*

The following sections describe the specimen preparation and the experimental procedure. More details of the experimental procedure, test-rig validation and the raw experimental data are available in Takaza and Simms (2012). However, in addition to the inverse modelling, significant additional experimental data for model verification are presented here.

2.1.1. *Specimen preparation and mechanical loading*

Freshly harvested porcine *Longissimus dorsi* samples were prepared from 3 month old female pigs. Preparation of specimens with a specific defined uniform shape was difficult due to the soft nature of the tissue and the interaction of the microstructural components of matrix and fibres, and this problem has been previously noted (Van Loocke et al., 2006). Samples were compressed either in the cross-fibre (face A or C in Fig. 1 Left) or the fibre direction (face B in Fig. 1 Left). Due to the difficulties involved in accurately cutting fresh muscle tissue, cross-fibre samples were approximately cubic, and for the fibre direction tests, the samples were cuboid with width and depth nominally at 20 mm to reduce buckling effects

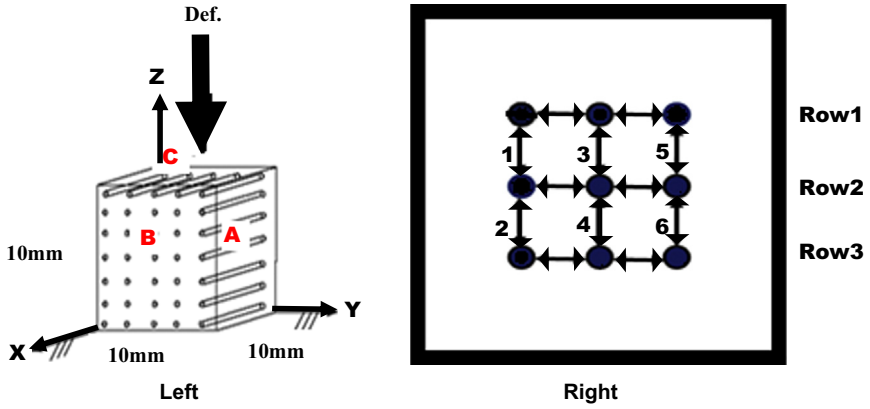

Fig. 1 – Left: schematic of a specimen illustrating the cross-fibre and fibre directions. The surfaces are marked A (cross-fibre direction), B (fibre direction) and C (cross-fibre direction). Right: schematic for the regions of interest used for strain analysis (reproduced from Takaza and Simms (2012)).

Table 1 – The experimental testing matrix (Takaza and Simms, 2012).

Testing direction	Specimen qty	Impact velocity (m/s)	Average specimen height (mm), mean and standard deviation	Strain rate %/s ($\dot{\varepsilon}_j$)
Cross-fibre	4	1.16	10.03±0.21	11,600
Cross-fibre	12	2.2	9.78±0.44	22,000
Cross-fibre	5	3.78	10.29±0.36	37,800
Fibre	5	2.2	10.27±0.38	22,000
Fibre	5	3.78	10.03±0.44	37,800

(Van Loocke et al., 2006; Van Sligtenhorst et al., 2006; McElhaney, 1966). Actual sample dimensions are shown in Table 1. Testing was performed within 2 h post-mortem to avoid the effects of rigor mortis (Van Loocke et al., 2006). A total of 31 compressive impact tests were performed at different strain rates in the fibre and cross-fibre direction as shown in Table 1 (Takaza and Simms, 2012). The above experiments were performed for a maximum compression of 30%. Each sample was tested only once, and sample mass before/after testing was used to record fluid expulsion. PTFE spray was used to lubricate the platen/muscle surface interactions to minimise friction effects.

2.1.2. *Derivation of experimental stress and deformation measures*

Each sample was marked with 9 dots on a side face prior to testing (using a black fine line waterproof pen (Mitsubishi, Uni-ball eye) as shown in Fig. 1 (right). The deformation of the marker dots was tracked using MATLAB (The Mathworks Inc., Natick, MA) based image analysis methods (Takaza et al., 2013). The strain for the overall deformation of the specimen was obtained using the platen displacement from the video data. For local deformations, the region of interest (see Fig. 1, right) was divided into 6 sub-regions and local stretch ratios (λ) were calculated by dividing the current height (marker-to-marker distance) (L_1) by the initial height(L_0):

$$\lambda = \frac{L_1}{L_0} \tag{1}$$

Engineering stress ($\mathbf{P}$) is presented in favour of Cauchy stress, as the deformation was not uniformly distributed from top to bottom of the sample due to inertial effects:

$$\mathbf{P} = \frac{\mathbf{F}_C}{A_0} \tag{2}$$

where (A_0)is the initial area in the undeformed state, and ($\mathbf{F}_C$) is the time varying compression force.

2.2. *Finite element modelling*

Simulation of the cross-fibre experimental tests was performed using finite element analysis (FEA) with the freely available FEBio software (version FEBio 1.5, MRL University of Utah (Maas et al., 2012)), and inverse analysis was performed using MATLAB based control and parameter optimisation.

2.2.1. *Finite element model description*

For simplicity, an idealised geometry model was used even though non-ideal geometries occurred in the experiment, see Table 1 (see Section 2.1.1). The muscle samples were represented by a $10\times10\times10$ mm^3 cube which was uniformly meshed using $10\times10\times10$ solid 4 node tri-linear hexahedral elements (total of 1000 elements). This was assumed to be a good average representation as some tissue dimensions were above as well below the ideal geometrical shape, see Table 1. This was found to have no influence in the optimised parameter as the input data were based on the averages experimental response and the shape standard deviation was low (see Table 1). The compression plate was meshed using 45×45 0.01 mm^2 thick quadrilateral shell elements (total 2025 elements) and assigned aluminium alloy (5251_H26) material properties (Young's Modulus=70 GPa, Poisson's ratio=0.35 and density=2780 kg/m^3). Contact between the compression plate and the sample top surface was modelled using a frictionless sliding interface (Ateshian et al., 2010; Al-Mayah et al., 2009) to replicate the experimental condition. A mesh convergence test was performed to determine the required mesh density (Chawla et al., 2009; Miller et al., 2000). The hourglassing parameter in FEBio was investigated in preliminary work (see Appendix) and it was established that a value of 15 effectively suppressed the hourglassing mode without significantly affecting the model response. In the simulations the muscle sample was subjected to dynamic unconfined compression by prescribing the compression plate displacement to match the experimental conditions for all three rates of testing (11,600%/s, 22,000%/s and 37,800%/s). An initial spacing of 0.2 mm between contact surfaces was used to allow the contact to develop.

2.2.2. *Constitutive modelling*

The constitutive modelling framework presented employs the following deformation metrics: $\mathbf{F}$, the deformation gradient tensor; $J=\det(\mathbf{F})$, the Jacobian or volume ratio; $\mathbf{C}=\mathbf{F}^T\mathbf{F}$, the right Cauchy–Green tensor and the principal stretches λ_i(with i=1,2,3). In addition, for uncoupled representations the following modified or deviatoric deformation metrics are $\tilde{\mathbf{C}}=J^{-2/3}\mathbf{C}=\tilde{\mathbf{F}}^T\tilde{\mathbf{F}}$ employed (denoted $\tilde{\bullet}$):$\tilde{F}=J^{-2/3}\mathrm{F}$, $\tilde{C}=J^{-2/3}C=\tilde{F}^T\tilde{F}$, and $\tilde{\lambda}_i=J^{-1/3}\lambda_i$.

2.2.2.1. *Elastic behaviour*. The elastic behaviour of muscle tissue was modelled using the following uncoupled hyperelastic strain energy density formulation:

$$\psi(\tilde{C},J)=\tilde{\psi}(\tilde{C})\ +\ U(J). \tag{3}$$

Here $\tilde{\psi}$ defines the deviatoric elastic response of muscle tissue and is defined as an isotropic non-linear hyperelastic 1st order Ogden constitutive law (Ogden, 1972), similar to Bosboom et al. (2001)

$$\tilde{\psi}(\tilde{\lambda}_1,\tilde{\lambda}_2,\tilde{\lambda}_3)=\frac{c}{m^2}\left(\tilde{\lambda}_1{}^m+\tilde{\lambda}_2{}^m+\tilde{\lambda}_3{}^m-3\right). \tag{4}$$

where the behaviour is dictated by the material parameters c and m. The volumetric contribution is given by

$$U(J) = \frac{K}{2}(\ln J)^2, \tag{5}$$

where the material parameter K is the the Bulk Modulus. To satisfy near incompressibility (Maas et al., 2012), a bulk modulus of 20 MPa was used, see Appendix. The tissue was prescribed a material density of 1060 kg/m^3 (Patel et al., 2003).

The second Piola–Kirchoff stress tensor ($\mathbf{S}$) for the elastic behaviour can be written as (Maas and Weiss, 2013)

$$\mathbf{S} = 2\frac{\partial \psi}{\partial \mathbf{C}} = 2\frac{\partial \tilde{\psi}}{\partial \mathbf{C}} + pJ\mathbf{C}^{-1} = J^{-2/3}Dev(\tilde{\mathbf{S}}) + pJ\mathbf{C}^{-1} \tag{6}$$

where use was made of the reference frame deviatoric operator Dev $(\blacksquare) = (\blacksquare) - \frac{1}{3}((\blacksquare):\mathbf{C})\mathbf{C}^{-1})$, $\tilde{\mathbf{S}} = 2(\partial\tilde{\psi}/\partial\tilde{\mathbf{C}})$ is the deviatoric second Piola–Kirchoff stress and p is a pressure term given by

$$p = \frac{\partial U}{\partial J} = \frac{K}{J}\ln J. \tag{7}$$

2.2.2.2. *Viscoelastic behaviour*. The viscoelastic behaviour of muscle tissue is modelled using discretised quasi-linear viscoelasticity (QLV) (Puso and Weiss, 1998; Maas and Weiss, 2013) combined with the uncoupled hyperelastic formulation. Since the viscoelastic behaviour is defined only for the deviatoric stress, the Second Piola–Kirchoff stress can be written as

$$\mathbf{S}(t) = J^{-\frac{2}{3}}\int_{-\infty}^{t} G(t-s)\frac{\partial(Dev(\tilde{\mathbf{S}}^e))}{\partial s}ds + pJ\mathbf{C}^{-1}, \tag{8}$$

where $(\tilde{\mathbf{S}}^e)$ is the pure elastic deviatoric Second Piola–Kirchoff stress, see Eq. (6). The function G defines a discretised relaxation function given by

$$G(t) \ = 1 + \sum_{i=}^{n} \gamma_i e^{-\frac{t}{\tau_i}} \tag{9}$$

where γ_i and τ_i define proportional and time decaying viscoelastic behaviour respectively and it is clear that the long-term deviatoric response reduces to the pure elastic response described earlier. In the modelling, a three-term relaxation function was employed. For a more detailed description, the reader is referred to Puso and Weiss (1998)) and (FEBio-Manuals-Version-1.5 (2012).

2.2.3. *Contact definition and boundary conditions*

The compression plate was prescribed a downward displacement to achieve an overall sample compression of 30% and the time taken was set to match the different experimental conditions. Vertical displacements of the nodes of the bottom surface of the muscle sample were constrained and the central node of the bottom surface was pinned to anchor the model. Predicted boundary condition force measurements were obtained from the reaction forces between the top surface of the muscle and the compression plate.

2.2.4. *Inverse optimisation based constitutive parameter identification*

The elastic and viscoelastic material parameters were fitted separately. First, the Ogden elastic parameters (c and m) were obtained in an initial optimisation run by simulating the quasi-static 0.05%/s cross-fibre direction experimental data from Van Loocke (Van Loocke et al., 2006). Next, the three viscoelastic time constants (τ_1, τ_2, τ_3) were fixed at 0.015 ms, 0.0015 ms and 0.00015 ms respectively to span the time interval of the experimental tests, similar to the approach of Van Loocke et al. (Van Loocke et al., 2008). The remaining three viscoelastic parameters $(\gamma_1, \gamma_2, \gamma_3)$ were then obtained through inverse analysis of the experimental cross-fibre tests at the three different compression rates $\dot{\varepsilon}_i$ ($\dot{\varepsilon}_1 = 11{,}600\%/s$, $\dot{\varepsilon}_2 = 22{,}000\%/s$ and $\dot{\varepsilon}_3 = 37{,}800\%/s$), where the elastic parameters (c and m) were fixed. The optimisation process was controlled through a custom MATLAB code (Moerman et al., 2013) which

(a) generated FEBio input files containing the model description and appropriate material parameters;
(b) started an FEBio simulation and imported results once analysis was terminated (e.g. simulated force curves);
(c) computed the sum of squared differences between simulated and experimental force/stretch ratio data which here served as the optimisation penalty parameter. The inverse optimisation routine was based on the Nelder–Mead simplex search algorithm (implemented using the MATLAB *fminsearch* function, see also Lagarias et al. (1998)). The objective function (ϑ) for optimisation was defined as

$$(C,m) = \sum_i \sum_j (F_{exp}(\lambda_i,\dot{\varepsilon}_j) - F_{sim}(\lambda_i,C,m,\dot{\varepsilon}_j))^2 \tag{10}$$

which describes the objective function as the sum of squared differences between the experimental (F_{exp}) and simulated force (F_{sim}) data across all stretch levels λ_i and all three strain rates $\dot{\varepsilon}_j$.

Convergence was defined as being achieved when the parameter variation was less than 3%. Parameter convergence was also investigated for different initial parameter values and results were insensitive to the initial guess. The model predictions were assessed in relation to the experimental results in two ways: comparison of the boundary condition force in the contact between the upper platen and the tissue sample and comparison of the displacements of the markers in the experiment and their equivalent location in the model.

3. Results

3.1. *Experimental data*

Due to the volume of data generated, typical results are shown in detail first and then a statistical description of the variability is presented. Previous analysis verified that the applied strain rate was constant (Takaza and Simms, 2012).

Biological fluids were observed to be expelled from the specimen cut ends during the experiment, with the fluid loss resulting in an average of 8% reduction of sample mass during the testing for both the fibre and cross-fibre direction.

A typical cross-fibre direction specimen deformation during compression is presented in Fig. 2 (compression applied to cut face C in Fig. 1, left). The top row (R1) shows a camera

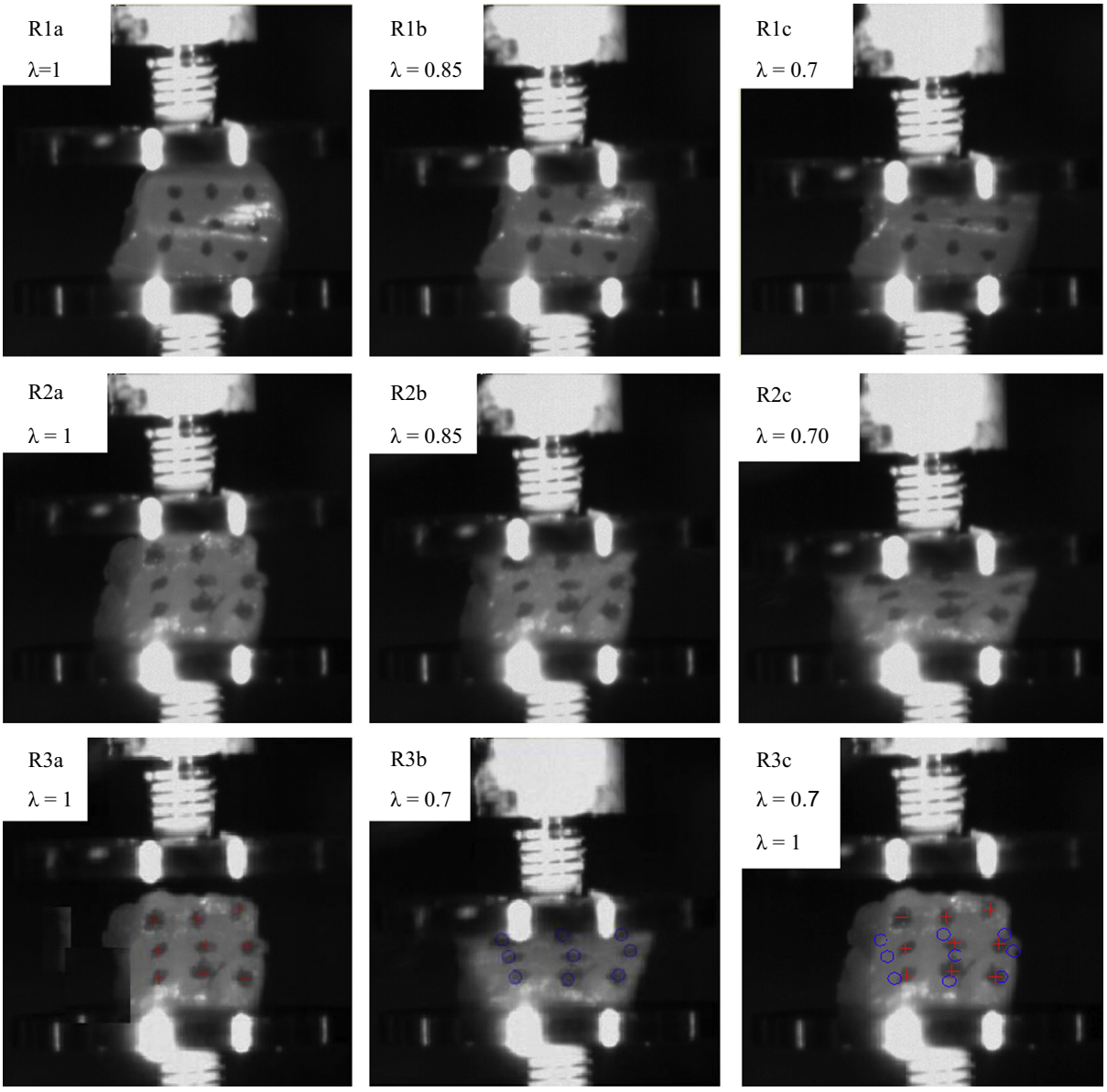

Fig. 2 – Cross-fibre experimental results: the first row (R1) shows the cross-fibre face (B in Fig. 2, left), the middle row (R2) shows the along fibre face (A in Fig. 1, left), and the bottom row shows the capability of the marker tracking algorithm in finding the marker centres in the initial (R3a shown as +) and final deformed state (R3b shown as o). The initial and final marker locations are overlaid on the un-deformed image in R3c. The overall applied stretch level is indicated by $\lambda = 0.7$ (reproduced from Takaza and Simms (2012)).

view on a face perpendicular to the muscle fibres (face B in Fig. 1, left). The middle row (R2) shows a camera view on a face parallel to the muscle fibres (face A in Fig. 1, left). Since only one high speed camera was used, the first row and second row in Fig. 2 represent images from tests on different samples. The bottom row shows the capability of the marker tracking algorithm to find the marker centres in the initial (R3a) and final deformed (R3b) state.

As can be seen from Fig. 2 (R1a), preparation of uniform samples is difficult due to the soft nature of the tissue. Accordingly, Fig. 2 shows that some shearing as well as axial compression occurred during the sample deformation. This is the result of a number of factors including the difficulty in preparing cubic specimens with an appropriate fibre orientation, the interaction of the microstructural components of matrix and fibres and the nature of the applied deformation.

These factors are evident from the strain history curves for the different regions presented in Fig. 3, which are typical individual specimen results for cross-fibre direction impacts. The left hand column shows the results when the load is applied in the cross fibre (face C in Fig. 1, left) and the displacement analysis is performed for the other cross-fibre face (face A in Fig. 1, left). The right hand column is when the load is still applied in the cross-fibre direction (face C in Fig. 1, left) but the displacement analysis is performed on the fibre direction face (face B in Fig. 1, left). The upper row of graphs represents the left hand column of marker dots, the middle

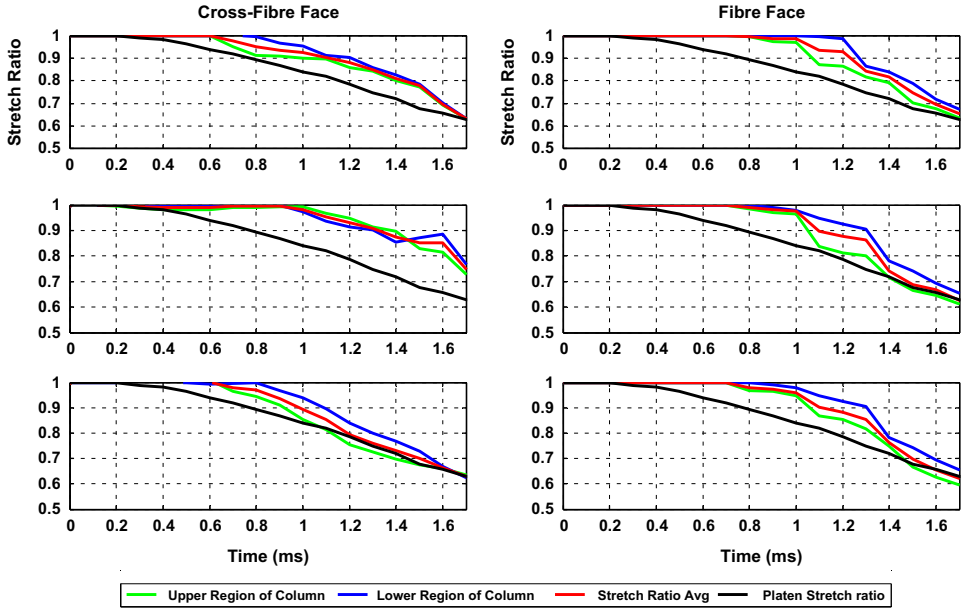

Fig. 3 – Typical strain variation within the regions of interest for a cross-fibre direction test (reproduced from Takaza and Simms (2012)). Regions that are marked by 1, 3 and 5 in Fig. 1 (right) are all in the top region. Regions marked by 2, 4 and 6 in Fig. 1 (right) are all in the lower regions.

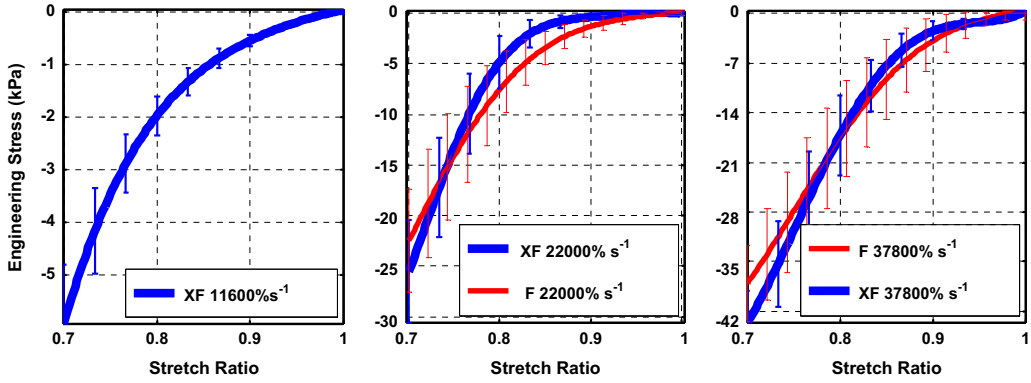

Fig. 4 – Summary of all experimental engineering stress–stretch ratio curves for loading in the fibre (F) and cross-fibre (XF) directions.

row represents the middle column of marker dots and the bottom row represents the right hand columns of marker dots.

Fig. 4 shows the resulting mean and standard deviation engineering stress versus stretch ratio results for all of the experimental tests, which were performed in the fibre and cross-fibre direction at 11,600%/s, 22,000%/s and 37,800%/s, see Table 1.

3.2. *Model results*

Table 2 shows the 1st order Ogden model parameters obtained through the inverse analysis processes and also the bulk modulus (held constant during optimisation) as well as the elastic parameters (c and m) obtained in the initial optimisation in simulating the quasi-static 0.05%/s cross-fibre direction experimental data from Van Loocke (Van Loocke et al., 2006).

Fig. 5 shows the experimental boundary condition force (mean and standard deviation) at the three testing rates together with the predicted FEA result for the optimised parameters in Table 2. Fig. 6 shows the experimental and optimised model shapes at peak compression at $\lambda=0.7$ for the three different testing rates. A comparison of the measured and predicted marker locations at peak compression is also shown (bottom row). Figs. 7 and 8 respectively show the measured versus predicted marker displacement time histories of the top, middle and bottom rows of markers on the sample for vertical and horizontal motion of the sample during compression.

4. Discussion

4.1. *Experimental*

Due to the paucity of data in the literature, the first goal of this work was to perform dynamic uniaxial compressive tests on uniformly shaped samples of freshly harvested skeletal

Table 2 – Optimised viscoelastic Ogden parameters.

γ_1	γ_2	γ_3	τ_1 (ms)	τ_2 (ms)	τ_3 (ms)	K (MPa)	c (MPa)	m
0.0715	2.49	0.277	0.015	0.0015	0.00015	20	0.001685	15.43

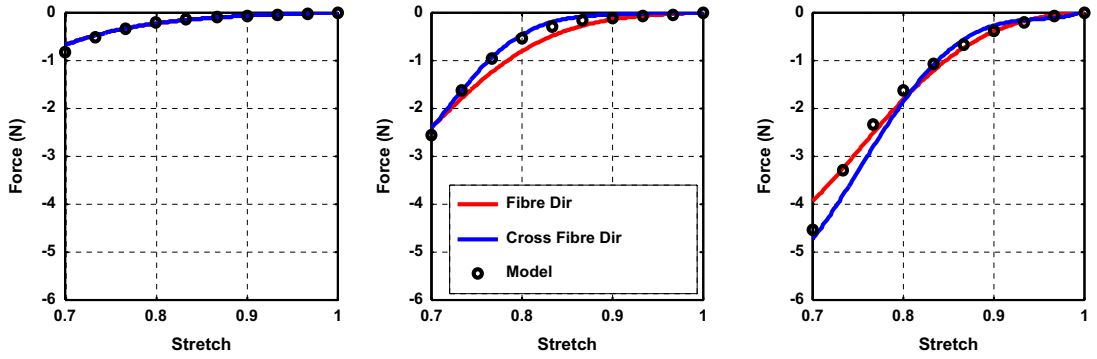

Fig. 5 – Comparison of the predicted model boundary condition force with experimental observation for cross-fibre direction tests at 11,600%/s, 22,000%/s and 37,800%/s using optimised model parameters. The red plots are the experimental fibre direction data, the blue is the cross-fibre experimental data and the black is the model predictions of the cross-fibre direction tests. (For interpretation of the references to color in this figure legend, the reader is referred to the web version of this article.)

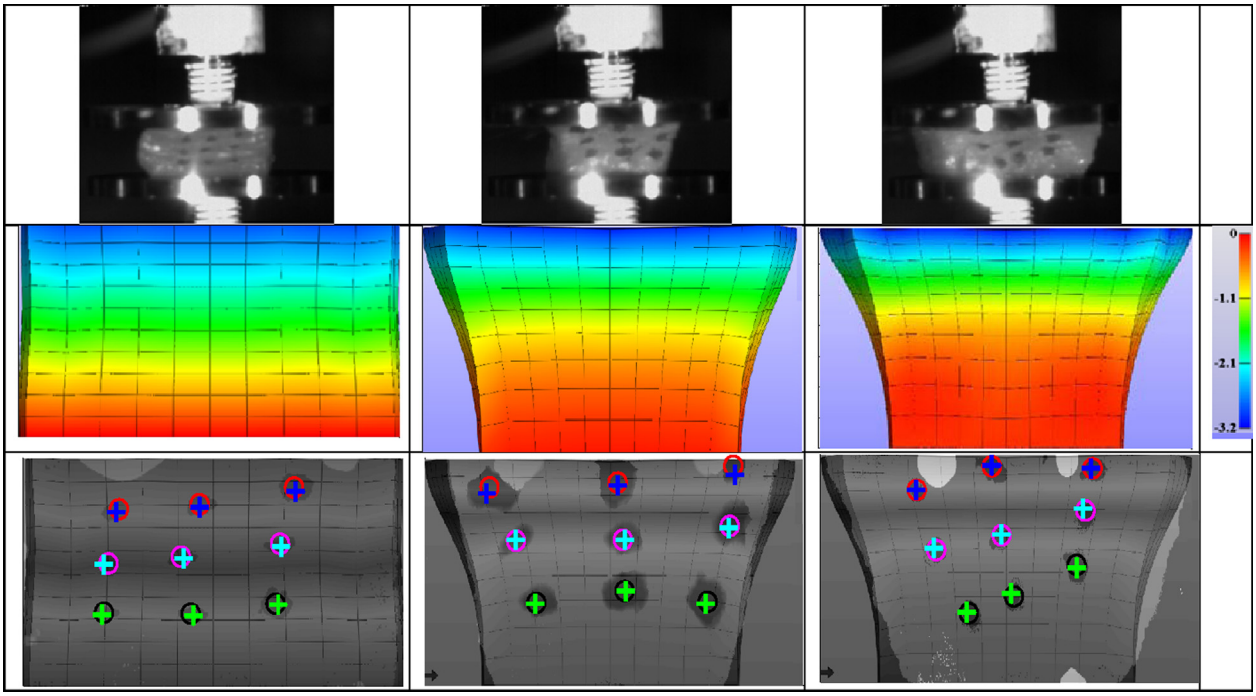

Fig. 6 – First row: images of the specimen at $\lambda = 0.7$ at testing rates of 11,600%/s, 22,000%/s and 37,800%/s. Second row: corresponding model image at 30% compression; the blue corresponds to the highest vertical displacement of 3.2 mm while the red colour shows areas with the least or no displacement at all. Third row: overlay of experimental test marker locations (o) and model predictions (+). (For interpretation of the references to color in this figure legend, the reader is referred to the web version of this article.)

muscle tissue in both the fibre and cross-fibre direction to define stress–stretch relationships at rates relevant to automotive injuries. Clearly, given the complex deformation behaviour observed, inverse analysis is necessary to extract material properties and the inverse FEA method was employed to achieve this.

Fig. 3 (left hand column) shows the typical evolution of strain in the different regions of the sample as a function of time for the cross-fibre direction tests when viewed orthogonal to the muscle fibres (face A in Fig. 1, left). The strain in the upper regions is initially greater than in the lower regions, but this equalizes towards the end of the test. Furthermore, the

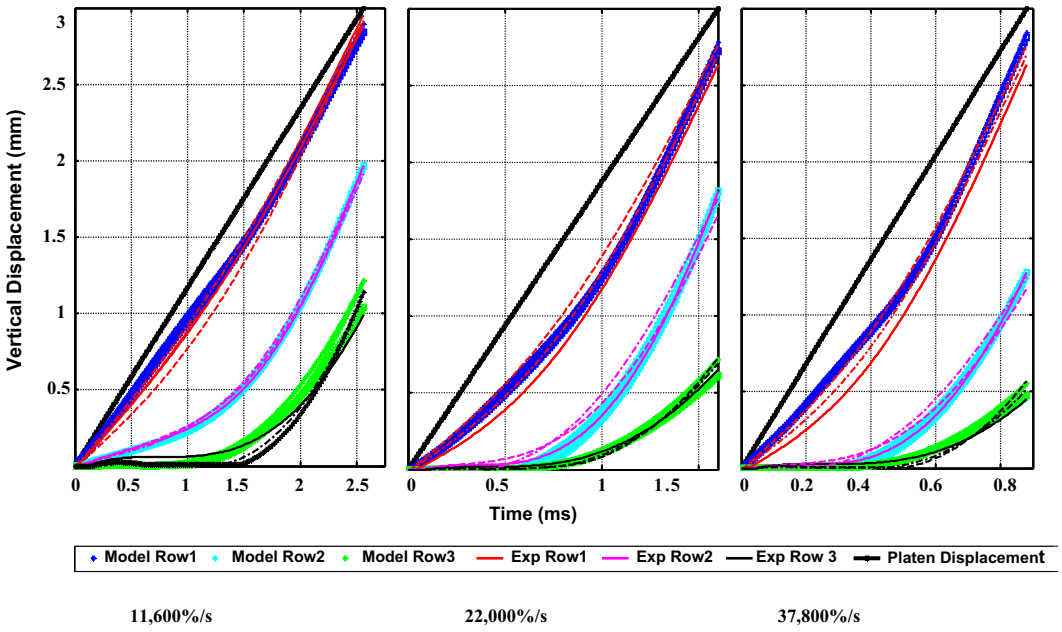

Fig. 7 – Comparison of average experimental and model vertical displacement of the 9 marker dots for cross-fibre direction tests at the 3 different strain rates (see Fig. 1, right for row identification).

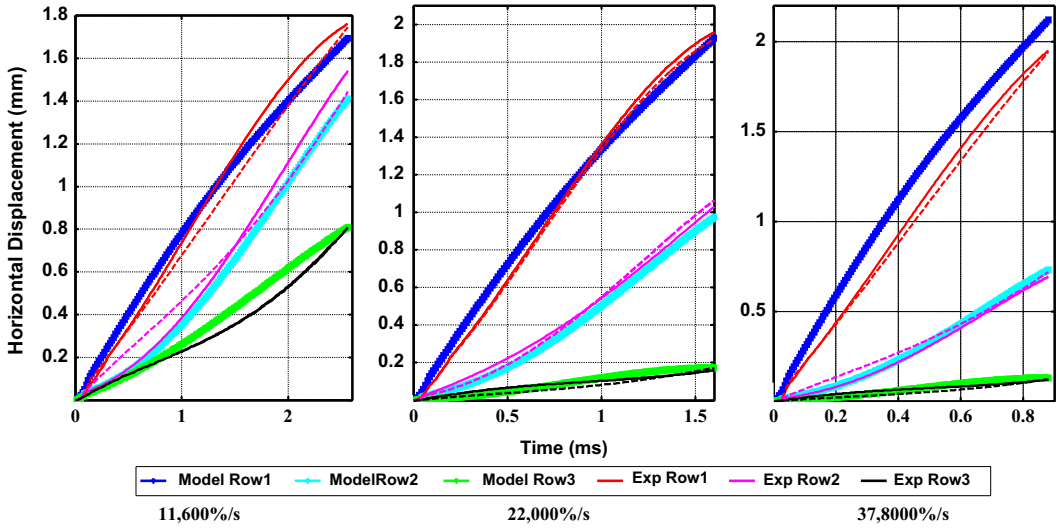

Fig. 8 – Comparison of average experimental and model horizontal displacement of the 9 markings for cross-fibre direction tests at the 3 different strain rates (see Fig. 1, right for row identification).

strain is greater at the left and right edges than in the middle of the sample. This may be because fluid expulsion is easier at the free boundaries, and the muscle fibres collapse earlier at these two edges (see face B in fig. 1, left). This could trap the fluid located at the specimen centre unless it can pass through the connective tissue matrix, and this is consistent with earlier lower rate results (Van Loocke et al., 2008), where the fluid expulsion appeared to be along, rather than across, the muscle fibres. The fluid loss resulted in an 8% reduction of sample mass on average during testing. Fig. 3 (right hand column) shows the equivalent results for a cross-fibre direction test when viewed parallel to the muscle fibres (face B in Fig. 1, left). It is again evident that the strain is initially greater at the top of the sample than at the bottom, but now the strain at the left and right edges is similar to the strain in the middle of the sample. These results highlight the dependency of the strain on the chosen region (see Fig. 1, right) and the results are significantly different from the stretch calculated from the platen displacements.

The engineering stress–stretch evaluations presented in Fig. 4 provide a starting point for the dynamic mechanical behaviour of fresh porcine skeletal muscle tissue in both the fibre and cross-fibre directions at automotive impact rates. The results show nonlinear stress–strain relationships as well as clear stiffening with increasing strain rate, which is similar to results from lower rate testing (Van Loocke et al., 2006;

Van Sligtenhorst et al., 2006; Song et al., 2007; Van Loocke et al., 2008; Chawla et al., 2009). The stress at 30% compression was approximately 9 times higher for the strain rate of 37,800%/s compared to 11,600%/s, which is qualitatively similar to observations at other strain rates (Van Loocke et al., , 2006, 2008; Zheng et al., 1999). The cross-fibre direction was observed to be more compliant than the fibre response at low stretch ratios and then stiffer at larger stretch ratios (see Fig. 5). This is similar to previous observations at different rates made by other authors if we only consider high strains (Van Loocke et al., 2008; Song et al., 2007; Van Loocke et al., 2006) but the differences observed between the fibre and cross-fibre direction responses were small and a one way ANOVA analysis showed the difference to be insignificant at $\alpha=0.05$.

Comparison to the published data is difficult as experimental protocols vary and there is no standard manner of presenting the experimental data. To enable comparison, for each experimental protocol, the stress at the lowest strain rate at $\lambda=0.7$ was taken as a reference and the ratios between this and the stress obtained at $\lambda=0.7$ for higher rates were calculated. The resulting stress ratios were then combined to show the increase in stress from a reference strain rate of 0.05%/s (which now gives a ratio of 1), see Fig. 9. In addition to data from the present paper, only data from Van Loocke (Van Loocke et al., 2006, 2008, 2009) and Song (Song et al., 2007) satisfied these requirements, see Fig. 9. The results of the present work show a continuous evolution in comparison with the Van Loocke et al. (2006, 2009) data (Van Loocke et al., 2006, 2007, 2008, 2009), but a higher stress response compared to the split Hopkinson bar results observed by Song et al. (Song et al., 2007), possibly due to the difference in testing protocol.

While Chawla et al. (2009) performed tests on human tissue at the relevant strain rates, they unfortunately used post-rigor mortis samples and did not report quasi-static results and so the evolution of strain rate effects cannot be readily assessed (Chawla et al., 2009). Direct comparison to the tests by Chawla et al. (2009) is also difficult as different strain rates were used, but a broad comparison shows that the stress at a stretch of 0.7 for the cross-fibre direction tests at both 11,600%/s and at 22,000%/s was about two to three times more compliant for the current tests than for the results of Chawla et al. (2009). This may be due to the effects of rigor mortis. As Chawla et al. (2009) did not test in the fibre direction, it is not possible to compare those results.

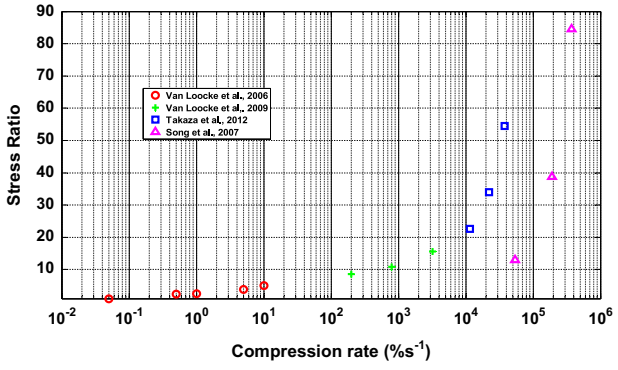

Fig. 9 – Relative increase in stress with compression rate at $\lambda=0.7$ for tests performed by Van Loocke et al. and Song et al. (Song et al., 2007; Van Loocke, 2007) and the experimental results from the current tests (reproduced from Takaza and Simms (2012)).

4.2. *The inverse FEA derived constitutive parameters*

Inverse optimisation was used to identify the viscoelastic material constants for a 1st order isotropic Ogden law expanded with a three term quasilinear viscoelastic (QVL) approach to capture rate dependent effects. The long term elastic parameters (c and m) in Table 2 were determined from the quasi-static cross-fibre data from Van Loocke et al (2006), for which the tissue was harvested from the same species and tested under similar experimental conditions. The main optimisation minimised the difference between the model boundary condition force and the experimental observations at all three testing rates (11,600%/s, 22,000%/s and 37,800%/s), see Table 2. When these optimised parameters were used (Table 2), the resulting predicted marker displacements of the marker locations matched the experimental results very well for all three testing rates, see Figs. 6–8 for vertical and horizontal deformations, even though an isotropic model was employed.

4.3. *Strengths and weaknesses*

In this paper, the experimental impact response of muscle tissue at rates relevant to automotive impacts is presented both in the fibre and the cross-fibre direction. This is the first time that the impact response of muscle tissue has been measured both in terms of the external boundary force and the tissue deformation measured at the cut faces. Parameter identification using the optimisation technique was performed only for the cross-fibre direction as it was observed that at high strain rates the muscle tissue behaved in a more or less isotropic manner, see Fig. 4. The inverse analysis shows that using a 1st order uncoupled viscoelastic Ogden material model with three relaxation branches a good response at each of the different strain rates can be obtained and, since the tissue anisotropy is relatively small at these dynamic loading rates, a good comparison to both the fibre and cross-fibre direction experimental results is achieved, see Fig. 5. A limitation of the finite element modelling is that the initial geometry of the muscle model was cuboid, while the experimental samples were only approximately cuboid due to difficulties in samples preparation, and this will have some influence on the predicted parameters (Bol et al., 2012). However, the parameters provided here provide a first step for finite element modelling of passive skeletal muscle during impact at rates relevant to automotive accidents.

The experimental data presented in this paper are also of use for future evaluation of constitutive models. In particular, the analysis presented in Figs. 7 and 8 showing the horizontal and vertical displacement time histories of the different regions in the sample provide a rich dataset for model evaluation.

Furthermore, we have shown an almost continuous evolution of stress ratio with strain rate by comparison with lower rate data from the literature, see Fig. 9. We have also shown that inverse FEA can be used to predict the passive muscle impact response at specific strain rates using a first

order uncoupled viscoelastic Ogden model. Nonetheless, the modelling should be developed in the future to incorporate anisotropy and the approach does not account for the tension compression asymmetry reported for muscle tissue (Gindre et al., 2013; Simms et al., 2012; Takaza et al., 2013) and additional viscoelastic terms will be required to capture effects over a larger frequency range.

5. Conclusions

In this paper we have provided fibre and cross-fibre direction stress–stretch data on the impact response of fresh passive porcine skeletal muscle tissue at rates between 11,600%/s and 37,800%/s, and these are relevant to automotive impacts. The detailed deformation response and boundary condition forces are presented for future finite element model evaluation. Furthermore, we have found an almost continuous evolution of stress ratio with strain rate by comparison with lower rate data from the literature. Inverse finite element analysis of the experiments, whereby muscle was represented by a 1st order Ogden hyperelastic model extended with a three term QVL expansion to account for rate dependent effects, indicated a good response at each of the different strain rates tested for both the boundary condition force and the tissue deformation observed. The Ogden model parameters are presented for future finite element modelling of the impact response of passive muscle tissue.

Acknowledgements

We would like to acknowledge Paul Normoyle for assistance with the LABVIEW data acquisition, as well as Peter O'Reilly and Mick Reilly for the technical advice they provided.

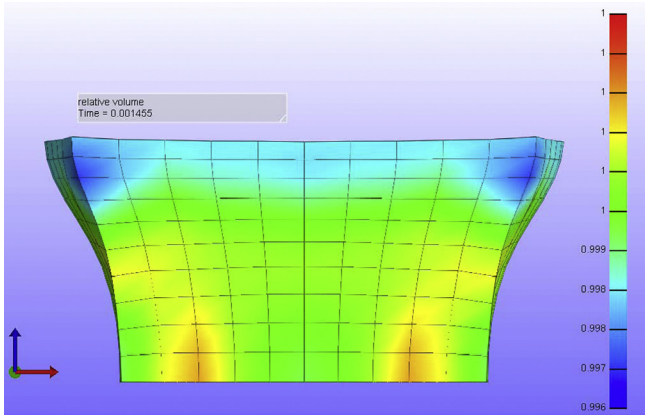

Fig. A3 – Volume preservation of the model at peak compression for Bulk Modulus $K=20$ kPa.

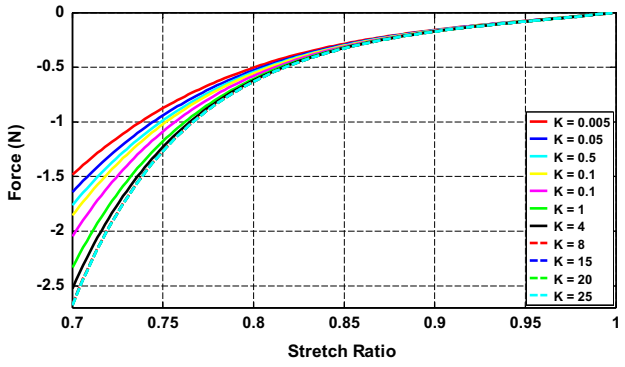

Fig. A1 – Influence of varying Bulk Modulus on boundary condition force versus muscle stretch.

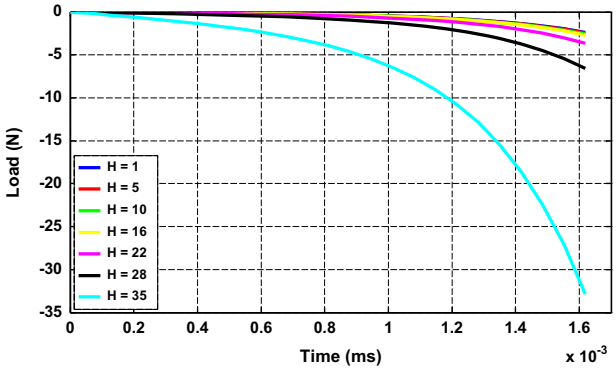

Fig. A4 – The effect on the boundary condition force time history of adjusting the hourglassing parameter (H).

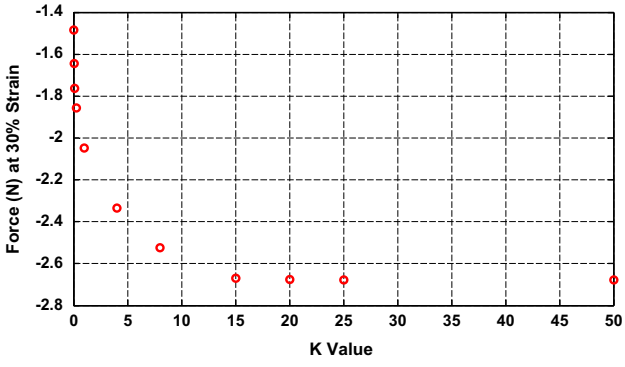

Fig. A2 – Influence of varying Bulk Modulus on peak boundary condition force at $\lambda=0.7$.

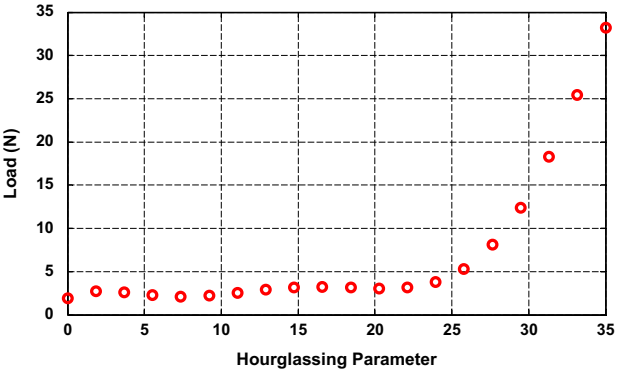

Fig. A5 – Influence of varying the hourglassing parameter (H) on peak boundary condition force at compression of $\lambda=0.7$.

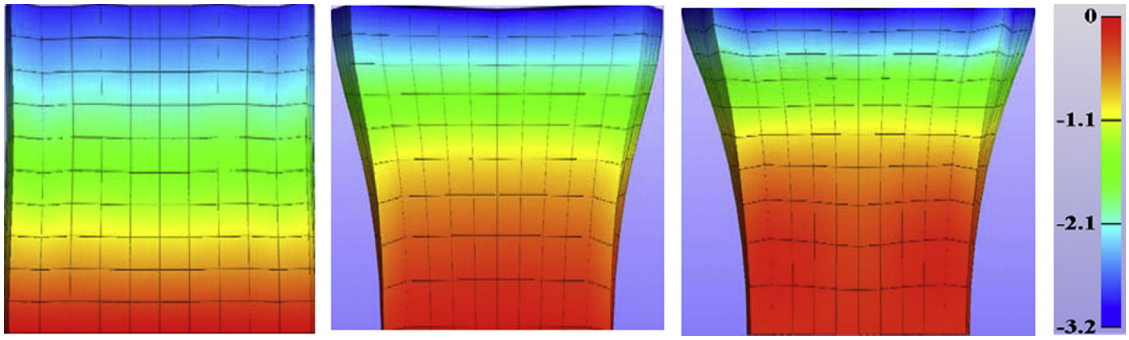

Fig. A6 – The predicted response of the model at each of the three simulated deformation rates when the hourglassing parameter (H) is set to 15 (the colours are displacements, with the blue colour being the highest vertical displacement and red being the least displacement).

Appendix: A

A1: Bulk modulus

The Bulk Modulus was investigated separately from the optimisation process to verify that incompressibility was achieved. Figs. A1 and A2 shows the effect of the Bulk Modulus parameter K on the boundary condition force at 30% compression: for a Bulk Modulus above 20 kPa the effect on the predicted boundary condition force is constant. Accordingly, the Bulk modulus was set to 20 kPa.

To verify that incompressibility was achieved when the Bulk modulus is 20 kPa, the relative volume was assessed, see Fig. A3 (below), which shows that when $K=20$ kPa, the relative volume is effectively 1 at the peak compression of $\lambda=0.7$, with the change of volume less than 0.5%.

A2: Hourglass mode suppression

The hourglassing parameter in FEBio was investigated after the final parameters were established through the optimisation process. The hourglassing parameter was gradually increased from zero, while the resulting boundary condition force was plotted against time, and the results are presented in Figs. A4 and A5 below.

Figs. A4 and A5 shows that the effect of the hourglassing parameter H on the boundary condition force is small when $H<15$, and this was therefore the value chosen for H. It is considered that this value provides effective hourglass mode suppression without significantly affecting the stiffness response of the tissue. The resulting deformation behaviour for $H=15$ at the three different impact rates is shown in Fig. A6.

Appendix: B Supporting information

Supplementary data associated with this article can be found in the online version at http://dx.doi.org/10.1016/j.jmbbm.2013.04.016.

REFERENCES

Al-Mayah, A., Moseley, J., Velec, M., Brock, K.K., 2009. Sliding characteristic and material compressibility of human lung: parametric study and verification. Medical Physics 36, 4625–4633.

Ateshian, G.A., Maas, S., Weiss, J.A., 2010. Finite element algorithm for frictionless contact of porous permeable media under finite deformation and sliding. Journal of Biomechanical Engineering 132, 061006.

Bol, M., Kruse, R., Ehret, A.E., Kay, L., Siebert, T., 2012. Compressive properties of passive skeletal muscle: the impact of precise sample geometry on parameter identification ininverse finite element analysis. Journal of Biomechanics 45, 2673–2679.

Bosboom, E.M., HESSELINK, M.K., Oomens, C.W., Bouten, C.W., Drost, C.V., Baaijens, F.P., 2001. Passive transverse mechanical proprties of skeletal muscles under in-vivo compression. Journal of Biomechanics 34, 1365–1368.

Chawla, A., Mukherjee, S., Karthikeyan, B., 2009. Characterisation of human passive muscles for imapct loads using genetic algorithm and inverse finite element methods. Biomechanics and Modeling in Mechanobiology 8, 67–76.

Chomentowski, P., Coen, P.M., Radikova′, Z., Goodpaster, B.H., Toledo, F.G.S., 2011. Skeletal muscle mitochondria in insulin resistance-differences in intermyofibrillar versus subsarcolemmal subpopulations and relationship to metabolic flexibility. Journal of Clinical Endocrinology and Metabolism 96, 494–503.

Dhaliwal, S.T., Beillas, P., Chou, C.C., Prasad, P., Yang, H.K., King, I. A., 2002. Structural response of the lower leg muscles in compression: a low impact energy study employing volunteers, cadavers and the hybrid III. Stapp Car Crash Journal 46, 229–243.

Maas, S., Rawlins, D., Jeffrey, W. Ateshian, G.A.(Eds.), 2012. FEBio 1.5 Theory and User Manuals, FEBIO-MANUALS-VERSION-1.5.

Gindre, J., Takaza, M., Moerman, K.M., Simms, C.K., 2013. A structural model of passive skeletal muscle shows two reinforcement processes in resisting deformation. Journal of mechanical Behaviour of Biomedical Materials 22, 84–94, http://dx.doi.org/10.1016/j.jmbbm.2013.02.007.

Han, Y., Yang, J., Mizuno, K., Matsui, Y, 2012. A study on chest injury mechanism and the effectiveness of a headform impact test for pedestrian chest protection from vehicle collisions. Safety Science 50, 1304–1312.

Kuwahara, S., Hosokawa, T., Okada, K., Mizuno, K., 2007. Finite Element Analysis of Pedestrian Lower Extremity Injuries in Car-to-Pedestrian Impacts. SAE Technical Paper.

Lagarias, J.C., Reeds, J.A., Wright, M.H., Wright, P.E., 1998. Convergence Properties of the Nelder–Mead Simplex Method in Low Dimensions. SIAM Journal on Optimization 9, 112–147.
Maas, S., Ellis, B., Ateshian, G., Weiss, J., 2012. FEBio: Finite Elements for Biomechanics. Journal of Biomechanical Engineering 134, 011005.
Maas, S. Weiss, J.A., 2013. FEBio Manuals and Theory.
Maeno, T. & Hasewaga, J. Development of a finite element model of the total human model for safety (THUMS) and application to car-pedestrian impacts. The 17th International Technical Conference on the Enhanced Safety of Vehicles, Amsterdam, 4–7 June 2001.
McElhaney, J.H., 1966. Dynamic response of bone and muscle tissue. Journal of Applied Physiology 21, 1231–1236.
Miller, K., Chinzei, K., Orssengo, G., Bednarz, P., 2000. Mechanical properties of brain tissue in-vivo: experiment and computer simulation. Journal of Biomechanics 33, 1369–1376.
Moerman, K.M., Nederveen, A.J., Simms, C.K., 2013. Image based model construction, boundary condition specification and inverse FEA control: a basic MATLAB toolkit for FEBio. Computer Methods in Biomechanics and Biomedical Engineeering (Salt Lake, Utah).
Muggenthaler, H., Von Merten, K., Peldshus, S., Holley, S., Adamec, J., Praxl, N., Graw, M., 2008. Experimental test for the validation of active numerial human models. Forensic Science International 177, 184–191.
Ogden, R.W., 1972. Large Deformation Isotropic Elasticity—On the Correlation of Theory and Experiment for Incompressible Rubberlike Solids. Proceedings of the Royal Society of London Series A, Mathematical and Physical Sciences 326, 565–584.
Patel, D.N., Jannapureddy, R.S., Hwang, W., Chaudhry, I., Boriek, A., 2003. Altered muscle force and stiffness of skeletal muscles in alpha-sarcoglycan-deficient mice. American Journal of Physiology–Cell Physiology 284, C962–C968.
Puso, M.A., Weiss, J.A., 1998. Finite element implementation of anisotropic quasilinear viscoelasticity using a discrete spectrum approximation. Journal of Biomechanical Engineering 120, 62–70.
Salem, R.O., Laposata, M., Rajenram, R., Cluette-Brown, J.E., Preedy, V.R., 2006. The total body mass of fatty acid ethyl esters in skeletal muscles following ethanol exposure exceeds that found in the liver and the heart. Alcohol and Alcoholism 41, 598–603.
Simms, C., Van Loocke, M., Lyons, C., 2012. Skeletal muscle in compression: modelling approaches for the passive muscle bulk. International Journal of Multiscale Computational Engineering 10, 143–154, http://dx.doi.org/10.1615/IntJMultCompEng.2011002419.
Song, B., Chen, W., Ge, Y., Weerasooriya, T., 2007. Dynamic and quasi-static compressive response of porcine muscle. Journal of Biomechanics 40, 2999–3005.
Takaza, M., Moerman, K.M., Gindre, J., Lyons, G., Simms, C.K., 2013. The anisotropic mechanical behaviour of passive skeletal muscle tissue subjected to large tensile strain. Journal of the Mechanical Behavior of Biomedical Materials 17, 209–220.
Takaza, M., Simms, C.K., 2012. The passive response of skeletal muscle to compressive impact loading. International Research Council on Biomechanics of Injury, p503 (Dublin) ⟨http://www.ircobi.org/downloads/2012contents.pdf⟩.
Van Loocke, M., 2007. Passive Mechanical Properties of Skeletal Muscle in Compression. Trinity College, Dublin (Ph.D. thesis).
Van Loocke, M., Lyons, C.G., Simms, C.K., 2006. A validated model of passive muscle in compression. Journal of Biomechanics 39, 2999–3009.
Van Loocke, M., Lyons, C.G., Simms, C.K., 2008. Viscoelastic properties of passive skeletal muscle in compression: Stress-relaxation behaviour and constitutive modelling. Journal of Biomechanics 41, 1555–1566.
Van Loocke, M., Simms, C.K., Lyons, C.G., 2009. Viscoelastic properties of passive skeletal muscle in compression–Cyclic behaviour. Journal of Biomechanics 42, 1038–1048.
Van Sligtenhorst, C., Cronin, D.S., Brodland, G.W., 2006. High strain rate compressive properties of bovine muscle tissue determined using a split Hopkinson bar apparatus. Journal of Biomechanics 39, 1852–1858.
Vignos, J.P.J., Lefkowitz, M., 1959. A biochemical study of certain skeletal muscle constituents in human progressive muscular dystrophy. Journal of Clinical Investigation 38, 873–881.
Zheng, Y., Mak, A.F.T., Lue, B., 1999. Objective assement of limb tissue elasticity; development of a manual indentation procedure. Journal of Rehabilitation Research and Development 36, 2.